

# Spiral Arms in Broad-line Regions of Active Galactic Nuclei

## I. Reverberation and Differential Interferometric Signals of Tightly Wound Cases

Jian-Min Wang<sup>1,2,3</sup>, Pu Du<sup>1</sup>, Yu-Yang Songsheng<sup>1</sup>, and Yan-Rong Li<sup>1</sup>

<sup>1</sup> Key Laboratory for Particle Astrophysics, Institute of High Energy Physics, Chinese Academy of Sciences, 19B Yuquan Road, Beijing 100049, China

<sup>2</sup> University of Chinese Academy of Sciences, 19A Yuquan Road, Beijing 100049, China

<sup>3</sup> National Astronomical Observatories of China, Chinese Academy of Sciences, 20A Datun Road, Beijing 100020, China

August 9, 2022

### ABSTRACT

As a major feature in spectra of active galactic nuclei, broad emission lines deliver information of kinematics and spatial distributions of ionized gas surrounding the central supermassive black holes (SMBHs), that is the so-called broad-line regions (BLRs). There is growing evidence for appearance of spiral arms in the BLRs. It has been shown by reverberation mapping (RM) campaigns that the characterized radius of BLRs overlaps with that of self-gravitating regions of accretion disks. In the framework of the WKB approximation, we show robust properties of observational features of the spiral arms. The resulting spiral arms lead to various profiles of the broad emission line. We calculate RM and differential interferometric features of BLRs with  $m = 1$  mode spiral arms. These features can be detected with high-quality RM and differential interferometric observations via such as GRAVITY onboard Very Large Telescope Interferometer. The WKB approximation will be relaxed and universalized in the future to explore more general cases of density wave signals in RM campaigns and differential spectroastrometry observations.

**Key words.** galaxies: active – quasars: emission lines – quasars: general – reverberation mapping

### 1. Introduction

Active galactic nuclei (AGNs) discovered by Seyfert (1943) are characterized by the appearance of prominent broad emission lines in their spectra (e.g., see the composite spectra in Vanden Berk et al. 2001 and Hu et al. 2012), which usually have full widths at half maximum (FWHM) of  $\gtrsim 10^3 \text{ km s}^{-1}$  or even a few  $10^4 \text{ km s}^{-1}$  (e.g., see reviews of Ho 2008; Netzer 2013). Such broad widths of emission lines undoubtedly indicate very deep potential wells in centers of AGNs first realized by Woltjer (1959), which directly motivated the establishment of the scenario that accretion onto supermassive black holes (SMBHs) powers the huge radiation energy of AGNs (Zel'Dovich 1965; Salpeter 1964; Lynden-Bell 1969). It is generally accepted that broad emission lines stem from BLR gas photoionized by ionizing photons emitted from accretion disks (Osterbrock & Ferland 2006). It has been made great progress in understanding AGN and quasar activities (e.g., Netzer 2013), but two major issues as to BLRs remain under debate so far: 1) origin of BLR gas; 2) structure and dynamics (see a brief review in Wang et al. 2017).

Thanks are given to reverberation mapping (RM) campaigns since 1980s, with the underlying principle proposed by Bahcall et al. (1972) and Blandford & McKee (1982). Photons of emission lines from structured ionized gas undergo different paths to observers, leading to time lags ( $\tau$ ) of the emission lines with respect to the ionizing photons. RM campaigns focusing on broad Balmer lines had detected the anticipated lags in a number of Seyfert galaxies (e.g., Peterson 1993; Peterson et al. 1998; Bentz et al. 2013; Barth et al. 2015; U et al. 2022) and quasars (e.g., Kaspi et al. 2000; Du et al. 2014, 2018a; Shen et al. 2019) in

the past decades. Along with the growing investment of observing resources and the development of analytical algorithms, the general geometry and kinematics of BLRs in some AGNs have been revealed by velocity-resolved delay analysis (e.g., Bentz et al. 2010; Denney et al. 2010; Grier et al. 2012, 2013; Du et al. 2016a; U et al. 2022), velocity-delay maps (e.g., Xiao et al. 2018; Horne et al. 2021), or dynamical modeling (e.g., Bottorff et al. 1997; Pancoast et al. 2014; Li et al. 2018; Williams et al. 2020). Many resolved BLRs have disk-like geometry of  $H\beta$  line region (the other have inflow or outflow, or a kind of mixture of the three configurations)<sup>1</sup>. Moreover, the repeated RM observations of the same emission line and the RM results of the emission lines with different ionization in a few AGNs (for instance NGC 5548, 3C 390.3, NGC 3783, NGC 7469, Mrk 817 etc.) approximately demonstrated a relation  $V_{\text{FWHM}} \propto \tau^{-1/2}$ , showing evidence for potential of SMBHs (e.g., Peterson & Wandel 2000; Peterson et al. 2004; Lu et al. 2021), where  $V_{\text{FWHM}}$  is the full-width-half-maximum of emission lines. Considering that disk-like geometry of BLRs in some AGNs, this relation probably indicates nearly Keplerian rotation of the disk BLRs. More recently, the GRAVITY instrument mounted in Very Large Telescope Interferometer (VLTI) spatially resolved the BLRs in several AGNs (e.g., 3C 273, NGC 3783, IRAS 09149 by Gravity Collaboration et al. 2018, 2020, 2021, respectively) and also found that their BLRs are approximately characterized by Keplerian rotating disks.

<sup>1</sup> It turns out that high-ionization lines, such as C IV line, favor origin from outflows. See Bottorff et al. (1997) for a first detailed study of C IV line in NGC 5548 observed by Hubble Space Telescope and International Ultraviolet Explorer.

Moreover, there is growing evidence for the existence of substructures or the inhomogeneity on the BLR disks from RM observations. For examples, a well-known phenomenon in RM is that the emission-line profiles in the mean spectra (corresponding to the entire region of line emission) and root mean square ones (RMS, to the portion of the region with response) are generally different in most AGNs (e.g., Bentz et al. 2009; Denney et al. 2009; Barth et al. 2013; Du et al. 2018b), which implies that the BLRs are inhomogeneous in terms of gas distributions. Furthermore, the sub-features in the velocity-delay maps of NGC 5548 (e.g., Xiao et al. 2018; Horne et al. 2021) indicate explicitly that there are probably gas inhomogeneity in BLRs. In particular, Horne et al. (2021) recently found helical “Barber-Pole” patterns in the Ly $\alpha$  and C iv lines of NGC 5548, which suggests azimuthal structures in their emitting regions. Multiple-peaked and asymmetric profiles of lines also indicate complicated BLR structures. These increasing pieces of evidence potentially suggest that there exist sub-structures in BLRs. Questions naturally arise: are the motions of the BLR sub-structures chaotic or ordered? What are their physical origin?

Motivated by the observational evidence, some preliminary efforts have been made that spiral arms are invoked to explain the asymmetric double-peaked broad emission lines, however, by only assuming some analytical form of the arm patterns without considering their physical origin or introducing any dynamical physics. These efforts were made by Gilbert et al. (1999) and Storchi-Bergmann et al. (2003, 2017) who adopted spiral arms to explain the asymmetric double-peaked emission lines and their variations in some AGNs. Horne et al. (2004) calculated the transfer function of BLRs with arms for RM, but all of them assumed some analytical forms of the spirals. All these mathematical models for observational data should be derived by the first principle in order to advance our understanding BLR physics.

The BLR radii measured by RM span from  $10^3 R_g$  to  $10^5 R_g$  depending on accretion rates and SMBH masses (see Figure 6 in Du et al. 2016b; Du & Wang 2019), which overlap with outer part of accretion disks, where  $R_g = GM_\bullet/c^2 = 1.5 \times 10^{13} M_8 \text{ cm}$  is the gravitational radius,  $G$  is the gravitational constant,  $c$  is speed of light, and  $M_8 = M_\bullet/10^8 M_\odot$  is the SMBH mass. Some pioneering works suggest that the outer regions may be self-gravitating (SG, e.g., Paczyński 1978a,b) for viscosity mechanism transferring angular momentum outward, in particular, in AGN accretion disks (see details of Shlosman & Begelman 1989). It is not difficult to give an rough estimate of the SG radius using the famous Toomre parameter  $Q = \kappa a / \pi G \sigma$  (Toomre 1964), which is the criterion of the instability, where  $\kappa$  is the epicyclic frequency (equal to the angular speed  $\Omega$  in a Keplerian disk),  $a$  is the sound speed, and  $\sigma$  is the surface density. Using  $Q = 1$ , Goodman (2003) approximated  $R_{SG}/R_g = 3.1 \times 10^3 \alpha_{0.1}^{2/9} (L_{\text{Bol}}/L_{\text{Edd}})^{4/9} M_8^{-2/9}$ , where  $\alpha_{0.1} = \alpha/0.1$  is the viscosity parameter and  $L_{\text{Bol}}/L_{\text{Edd}}$  is the Eddington ratio. Interestingly, SG part of the disks spatially overlap BLRs generally in AGNs, and this motivates that BLR structures and dynamics link with SG part somehow.

The ultimate fates of the SG accretion disks remain a matter of debate, however self-regulation processes, balanced by radiation cooling and the heating internally from the dissipation of gravito-turbulence (e.g., Paczyński 1978a,b; Lin & Pringle 1987; Gammie 2001; Lodato & Rice 2004) and probably also magneto-rotational instabilities (MRI, e.g., Balbus & Hawley 1998; Rafikov 2015), or externally from irradiation (driven by the inner part of accretion disk, e.g., Rice et al. 2011; Rafikov

2015) or star formation (inside the disks, e.g., Collin & Zahn 1999; Sirko & Goodman 2003; Wang et al. 2011), are believed to maintain the disks so that they can stay in marginally stable states. In such states, non-axisymmetric perturbations (spiral structures) may inevitably grow in the SG parts, although clumps or stars may also form through condensations if the cooling time scale  $t_{\text{cool}} < \beta \Omega^{-1}$ , where  $\beta$  is a factor of a few (e.g., Gammie 2001; Rice et al. 2003, 2011; Kratter & Lodato 2016; Brucy & Hennebelle 2021). The aforementioned phenomenological evidences of BLR substructures and inhomogeneity enlighten us that they may be connected with or originated from the spiral arms in the SG part of accretion disks, at least for those AGNs with disk-like BLRs.

As the first paper of this series, we adopt the simple tight-winding approximation and use analytical formulations to discuss the observational characteristics of tightly wound cases of density waves in BLRs. The basic formulations, equilibrium states, and boundary conditions are provided in Section 2. In Section 3, observational features of the arms are discussed for RM campaigns and interferometric observations of GRAVITY/VLTI. Brief discussions and conclusions are provided in Section 4 and 5, respectively. It should be noted that the purpose of this paper is to demonstrate the general features of BLR spiral arms in observations (e.g., RM) rather than establish a perfect model.

## 2. Model and Formulations

In the BLR, the ionized gas is rotating with nearly Keplerian velocity around the central SMBH. This assumption is supported by the evidence that  $V_{\text{FWHM}}$  and  $\sigma_\ell$  are roughly proportional to  $\sim \tau_{\text{H}\beta}^{-1/2}$  in some AGNs from the multiple RM campaigns (Peterson et al. 2004; Lu et al. 2021), where  $\sigma_\ell$  is velocity dispersion of the H $\beta$  profiles in the RMS spectra, respectively, and  $\tau_{\text{H}\beta}$  are the H $\beta$  time lags with respect to the 5100Å continuum variations. However, current accuracy of RM data doesn’t allow us to quantitatively determine deviations from exactly Keplerian rotation, it should be reasonable to assume the disk-BLR has nearly Keplerian. As one of possible mechanisms, the magneto-rotational instability (MRI) (e.g., Balbus & Hawley 1998) drives radial motion with velocity approximated by  $u/u_K \approx 0.1\alpha_{0.1}$  which is much smaller than the rotation, where  $u_K$  is the Keplerian rotation. Moreover, for the disks dominated by the central point masses, weak self-gravity of the disks can still maintain spiral arms (e.g., Lee & Goodman 1999; Tremaine 2001).

In this paper, for simplicity, we apply the classic theory of density waves (e.g., Lin & Shu 1964, 1966; Lin & Lau 1979) to calculating the broad-emission-line profiles and the transfer function for RM, and the differential phase curve signal for GRAVITY/VLTI.

### 2.1. Self-gravitating disk and BLR

Following Paczyński (1978a), without specifying regulation mechanisms (dusty gas, star formation, photoionization and accretion etc.), we use the polytropic relation as a prescription of  $Q_{\text{disk}} \sim 1$  region for general cases, which is given by  $p = K_0 \rho^{1+1/n}$ , where  $p$  is the pressure,  $\rho$  is the density,  $K_0$  is a constant, and  $n$  is the polytropic index. Fortunately,  $K_0$  can be generally constrained by observations of the BLR geometry. The sound speed is given by  $a_0 = (p/\rho)^{1/2} = K_0^{1/2} \rho^{1/2n}$ . The vertical equilibrium admits  $H = a_0 \Omega^{-1}$ , and the Toomre parameter is given by  $Q_{\text{disk}} = \kappa a_0 / \pi G \sigma_0$ , where  $\sigma_0 = 2\rho H$  is the surface den-

sity of the SG region. Here we would like to point out that self-gravity is neglected for vertical equilibrium for simplicity. The epicyclic frequency is given by  $\kappa = 2\Omega \left(1 + \frac{1}{2} \frac{d \ln \Omega}{d \ln R}\right)^{1/2} \approx \Omega$ , and we adopt a Keplerian velocity here that  $\Omega = \sqrt{GM_\bullet/R^3} \approx 2 \times 10^{-9} M_8^{-1} r_4^{-3/2} \text{ s}^{-1}$ . We have

$$a_0 = \frac{K_0^{1/2}}{(2\pi G Q_{\text{disk}})^{1/2n}} \Omega^{1/n}, \quad (1)$$

$$\sigma_0 = \frac{2K_0^{1/2}}{(2\pi G Q_{\text{disk}})^{(1+2n)/2n}} \Omega^{(1+n)/n}, \quad (2)$$

and

$$H = \frac{K_0^{1/2}}{(2\pi G Q_{\text{disk}})^{1/2n}} \Omega^{(1-n)/n}. \quad (3)$$

Given  $n$ ,  $K_0$  and  $Q_{\text{disk}}$ , we can drive the radial structures of BLR.

The polytropic index  $n$  is a free parameter in this paper, of which the value can be  $0 \sim +\infty$ . In practice, for instance, Paczyński (1978a) discussed the SG disks with  $n = 1.5$  and 3, Lubow & Ogilvie (1998) chose  $n = 3$  in their work, and Korycansky & Pringle (1995) employed  $n = 5$  as a typical case in the discussion of axisymmetric waves in accretion disks. In the present paper, the polytropic index  $n$  controls the radius-dependent thickness of the gaseous disk, i.e.,  $H/R \propto R^{(n-3)/2n}$ . If  $n > 3$ , the disk becomes thicker at outer radius and the surface of the disk tend to be “bowl-shaped” (similar to Goad et al. 2012). The bowl shape enables the gas on the disk surface to be illuminated by the ionizing photons from the inner part of the disk, otherwise, the geometrically thin disks are not able to be sufficiently ionized.

Observational constrains on BLR gas indicate that the BLR mass of H $\beta$ -emitting gas could be in a wide range from  $10^3 \sim 10^4 M_\odot$ , and even more massive (Baldwin et al. 2003). As a simple estimation, we integrate the surface density of the SG part of accretion disks and obtain a mass of  $M_{\text{disk}} \approx 4.1 \times 10^6 \alpha_{0.1}^{-4/5} M_8^{11/5} \mathcal{M}^{7/10} r_4^{5/4} M_\odot$  in light of the standard model of accretion disks (Shakura & Sunyaev 1973), where  $\mathcal{M} = \dot{M}_\bullet / \dot{M}_{\text{Edd}}$  is the dimensionless accretion rates,  $\dot{M}_\bullet$  is the mass accretion rates,  $\dot{M}_{\text{Edd}} = L_{\text{Edd}}/c^2$  is the Eddington rates, and  $L_{\text{Edd}} = 1.3 \times 10^{46} M_8 \text{ erg s}^{-1}$  is the Eddington luminosity. This indicates that the BLRs are the disk surface taking only tiny fraction of this SG portion. In the present paper, we assume that the ionized BLR gas is proportional to the density of the disk  $\rho_{\text{ion}} \propto \rho$  (see the following Section 2.3). It is found that  $M_{\text{disk}}/M_\bullet \ll 1$ , namely, the accretion disks are much lighter than the central SMBH unless for cases with extremely super-Eddington accretion rates ( $\mathcal{M} \gg 1$ ). Though  $\mathcal{M} \sim 900$  AGNs have been found from RM campaigns (Du et al. 2014, 2016a,b, 2018a), we limit the present scope for sub-Eddington accretion disks ( $\mathcal{M} \lesssim 3$ ) with nearly Keplerian rotation of a point potential of SMBH mass.

We would point out here a possibility that enough high density outflows emitting high ionization lines could partially shield the outer part of BLRs making reverberation of H $\beta$  line complicated (Dehghanian et al. 2019). If it happens in such a case, H $\beta$  line would undergo a holiday driven by the inner outflows (of C iv line) like in NGC 5548 (see Figure 7 in Pei et al. 2017), namely, appearing a lack of reverberation. However, H $\beta$  line only had the holiday once over the last 20 years (Pei et al. 2017), indicating that such a holiday is quite rare and the obscurations are not common.

## 2.2. Equations and boundary conditions

### 2.2.1. Perturbation equations

We adopt the formalisms and notations used in Lin & Lau (1979). For an  $m$ -fold axisymmetric perturbation,  $(u, v, \sigma) = (u_0, v_0, \sigma_0) + (u_1, v_1, \sigma_1)e^{i(\omega t - m\varphi)}$ , where  $u$  and  $v$  are the radial and azimuthal velocities, and  $\sigma$  is the surface density. The parameters with subscript “0” correspond to the equilibrium state (we take  $u_0 = 0$  in this paper), which are functions of radius. We have the perturbation of the equations given in Appendix A,

$$\frac{1}{R} \frac{d}{dR} (R \sigma_0 u_1) - \frac{im}{R} \sigma_0 v_1 + i(\omega - m\Omega) \sigma_1 = 0, \quad (4)$$

$$i(\omega - m\Omega) u_1 - 2\Omega v_1 = -\frac{d(\psi_1 + h_1)}{dR}, \quad (5)$$

and

$$\frac{\kappa^2}{2\Omega} u_1 + i(\omega - m\Omega) v_1 = im \frac{\psi_1 + h_1}{R}, \quad (6)$$

yielding the following differential equation

$$\frac{d^2}{dR^2} (h_1 + \psi_1) + \mathcal{A} \frac{d}{dR} (h_1 + \psi_1) + \mathcal{B} (h_1 + \psi_1) = -Ch_1, \quad (7)$$

where  $h_1 = a_0^2 \sigma_1 / \sigma_0$ . Here the coefficients  $\mathcal{A}, \mathcal{B}, C$  are given in Appendix B.

The Poisson equation of the SG portion of the accretion disks reads  $\nabla^2 \psi = 4\pi G \sigma \delta(z)$ , through vertical integration, yielding

$$\frac{d\psi_1}{dR} = -\frac{\psi_1}{2R} - is_k \Sigma h_1, \quad (8)$$

where  $\delta(z)$  is the Dirac- $\delta$  function,  $\Sigma = 2\pi G \sigma_0 / a_0^2$ , and  $s_k = \mp 1$  is the sign function of wave vector ( $k$ ) for trailing and leading waves, respectively. The Poisson equation holds approximately in the order of  $(H/R)^2$ . Combining the perturbation equations, we have the equation of the reduced enthalpy ( $U$ )

$$\frac{d^2 U}{dR^2} + k_3^2 U = 0, \quad (9)$$

where

$$U = h_1 \left[ \frac{\kappa^2 (1 - \nu^2)}{\sigma_0 R} \right]^{-1/2} \exp \left( \frac{i}{2} \int \Sigma dR \right), \quad (10)$$

and

$$k_3^2 = \left( \frac{\kappa}{a_0} \right)^2 (Q_{\text{disk}}^{-2} - 1 + \nu^2); \quad \nu = \frac{\omega - m\Omega}{\kappa}. \quad (11)$$

Bertin (2014) presents more detailed derivations of the above equations (7 and 9). Equation (9) works approximately in the order of  $H/R$ , which agrees with that of the Poisson equation. As a first application of density waves in BLR, we retain this order of approximation for simplicity.

### 2.2.2. Boundary conditions

In the context of spiral galaxies, the outer boundary conditions are imposed by radiation condition (Lin & Lau 1979). Considering that dynamics of dusty and dust-free gas will be very different due to radiation pressures (either from local or central part) of accretion disks. The boundary could be distinguished by the dust sublimation radius. For the present SG disk, the outer boundary is fixed at the inner edge (inward is dust-free) of dusty torus where the waves are evanescent. Although the dusty torus is generally not spatially resolved (except for NGC 1068 which shows a near-infrared cavity with a sharp edge in Gravity Collaboration 2020), fortunately, the RM campaigns of near-infrared continuum emissions show that the inner edge of torus is about  $R_{\text{torus}} \approx 0.1 L_{43.7}^{0.5} \text{ pc}$  (Suganuma et al. 2006; Koshida et al. 2014; Minezaki et al. 2019; Lyu et al. 2019), where  $L_{43.7}$  is the V-band luminosity in units of  $10^{43.7} \text{ erg s}^{-1}$  (see the latest version in Minezaki et al. 2019). It was long believed that the out edge of BLR is just the inner edge of torus (e.g., Netzer & Laor 1993; Suganuma et al. 2006; Czerny & Hryniewicz 2011). Therefore, we can obtain the outer radius of the BLR

$$R_{\text{out}} = 205.9 \eta_{0.1}^{1/2} \epsilon_{10}^{-1/2} \mathcal{M}^{1/2} M_8^{1/2} \text{ ltd}, \quad (12)$$

from  $R_{\text{out}} = R_{\text{torus}}$ , the bolometric luminosity is  $L_{\text{Bol}} = \epsilon L_V = \eta \mathcal{M} \dot{M}_{\text{Edd}} c^2$ ,  $\epsilon = 10 \epsilon_{10}$  is the bolometric luminosity correction factor and  $\eta = 0.1 \eta_{0.1}$  is the radiative efficiency. This agrees with the observation of NGC 1068 (Gravity Collaboration 2020) by GRAVITY onboard VLTI. We adopt a vanishing perturbation of density at the outer boundary. For the simplest case of the inner boundary, we assume

$$\frac{dU}{dR} = 0, \quad (13)$$

just as in Lau & Bertin (1978). We set the inner radius to be 10 percent of the outer radius, and have checked that the detailed value of inner radius does not change the general features of spiral arms. With the boundary conditions, it becomes an eigenvalue problem to solve Eqn (9). Then, we can obtain the perturbation of the surface density (more details can be found in, e.g., Lau & Bertin 1978; Lin & Lau 1979).

It should be pointed out that outer boundary conditions could be revised for individual AGNs if the spatially resolved conditions are different from the present. The adopted conditions are obvious that any  $H\beta$  photons will be extinguished by dusty gas within the torus whatever it is a kind of outflows (Königl & Kartje 1994; Elitzur & Shlosman 2006), clumpy structures (Nenkova et al. 2008) or classical continue torus (Antonucci 1993). On the other hand, accretion disks could extend outward and correspond to the mid-plane of torus, and density waves also extend (but depends on the local radiation pressure). In some AGNs, ALMA (Atacama Large Millimeter/submillimeter Array) observations show spiral arms, like in a few Seyfert galaxies (Combes et al. 2019), and it would be interesting to test if they are consistent with ones in BLRs. Recent interferometric observations of NGC 1068 show much more complicated structure (Gómez Rosas et al. 2022) as well as the counter-rotating disk from 0.2 to 7 pc by ALMA observations (Imanishi et al. 2018; Impellizzeri et al. 2019). In this paper, the simplest conditions are taken for the outer boundary physics.

### 2.3. Line profiles and 2-dimensional transfer functions

The emissivity distributions in BLRs are still unclear from observations. From photoionization, the locally optimally emitting

clouds model suggests that the line emission irradiates the most efficiently from a relatively narrow range of ionization parameter  $U_{\text{ion}} = Q_{\text{ion}}/4\pi R^2 c n_{\text{ion}}$ , where  $Q_{\text{ion}}$  is the number of ionization photons,  $n_{\text{ion}} = \rho_{\text{ion}}/m_{\text{H}}$  is the number density of hydrogen,  $\rho_{\text{ion}} \propto \rho = [\sigma_0(R) + \sigma_1(R, \varphi)]/2H = [\sigma_0(R) + \sigma_1(R, \varphi)] \Omega/2a_0$  is the ionized hydrogen density and assumed to be proportional to the density of the disk, and  $m_{\text{H}}$  is the mass of hydrogen atom (Baldwin et al. 1995; Korista et al. 1997; Korista & Goad 2000). For simplicity, we assume that the emissivity (reprocessing coefficient) is a Gaussian function of ionization parameter as

$$\Xi_R \propto \frac{1}{\sqrt{2\pi}\sigma_U} e^{-(U_{\text{ion}} - U_c)^2/2\sigma_U^2}, \quad (14)$$

where  $U_c = U_{\text{ion}}(R_c)$  is the ionization parameter corresponding to the most efficient line emission at radius  $R_c$  and  $\sigma_U = \tilde{\sigma}_U \times (U_{\text{ion,max}} - U_{\text{ion,min}})$  is a parameter that controls the range of line emission. Actually, the form of Eqn. (14) is one simplified version of the popular model (e.g., Pancoast et al. 2014; Li et al. 2018). The typical BLR radii are on average smaller than the inner edges of tori by factors of  $4 \sim 5$  (Koshida et al. 2014; Minezaki et al. 2019), thus we adopt  $R_c = 1/4 R_{\text{torus}}$  and assume  $\tilde{\sigma}_U = 0.20$  (corresponding to a not very compact line-emitting region).

Given the configuration of the disk-like BLR in Section 2.1, the emission-line profile can be expressed as

$$F_\ell(\lambda) = \int_{R_{\text{in}}}^{R_{\text{out}}} R dR \int_0^{2\pi} d\varphi \Xi_R \delta \left[ \lambda - \lambda_0 \left( 1 + \frac{\mathbf{v} \cdot \mathbf{n}_{\text{obs}}}{c} \right) \right], \quad (15)$$

where  $\mathbf{v}$  is the velocity of emitting gas,  $\mathbf{n}_{\text{obs}} = (0, \sin i_0, \cos i_0)$  is the vector of line of sight, and  $i_0$  is the inclination angle. Blandford & McKee (1982) developed the linear reverberation technique to map BLRs. Denoting the ionizing continuum light curve and broad-line light curve at velocity  $v$  of the line profile as  $L_c(t)$  and  $L_\ell(v, t)$ , respectively, we have

$$L_\ell(v, t) = \int_{-\infty}^{\infty} dt' L_c(t') \Psi(v, t - t'), \quad (16)$$

where  $\Psi(v, t)$  is the 2D transfer function (velocity-delay map),  $\Psi(v, t) = 0$  for  $t < 0$  and  $\Psi(v, t) \geq 0$  for  $t \geq 0$ . RM campaigns obtain  $L_\ell(v, t)$  and  $L_c(t)$ , which can be used to infer  $\Psi(v, t)$ . With the geometric and kinematic configurations of BLRs with density waves, the 2D transfer function can be obtained by

$$\Psi(v, t) = \int d\mathbf{R} \frac{g(\mathbf{R}, v)}{4\pi R^2} \Xi_R \delta \left[ t - \frac{(R + \mathbf{R} \cdot \mathbf{n}_{\text{obs}})}{c} \right], \quad (17)$$

where  $g(\mathbf{R}, v)$  is the projected one-dimensional velocity distribution function. With Equation (17), features of density waves can be calculated and then compared with observations.

In principle, high fidelity data from RM campaigns can be used to generate 2D transfer functions through the maximum entropy (Horne et al. 2004) or the improved Pixon-based method (Li et al. 2021). Spiral arms as prominent inhomogeneous components of BLRs can be directly tested avoiding uncertainties of explanations in light of complicated profiles alone.

### 2.4. Signals for GRAVITY/VLTI

As a powerful technique, spectroastrometry (SA) developed from ‘‘Differential Speckle Interferometry’’ (Beckers 1982; Petrov 1989; Rakshit et al. 2015) measures the center of photons and therefore greatly improve the spatial resolution. The

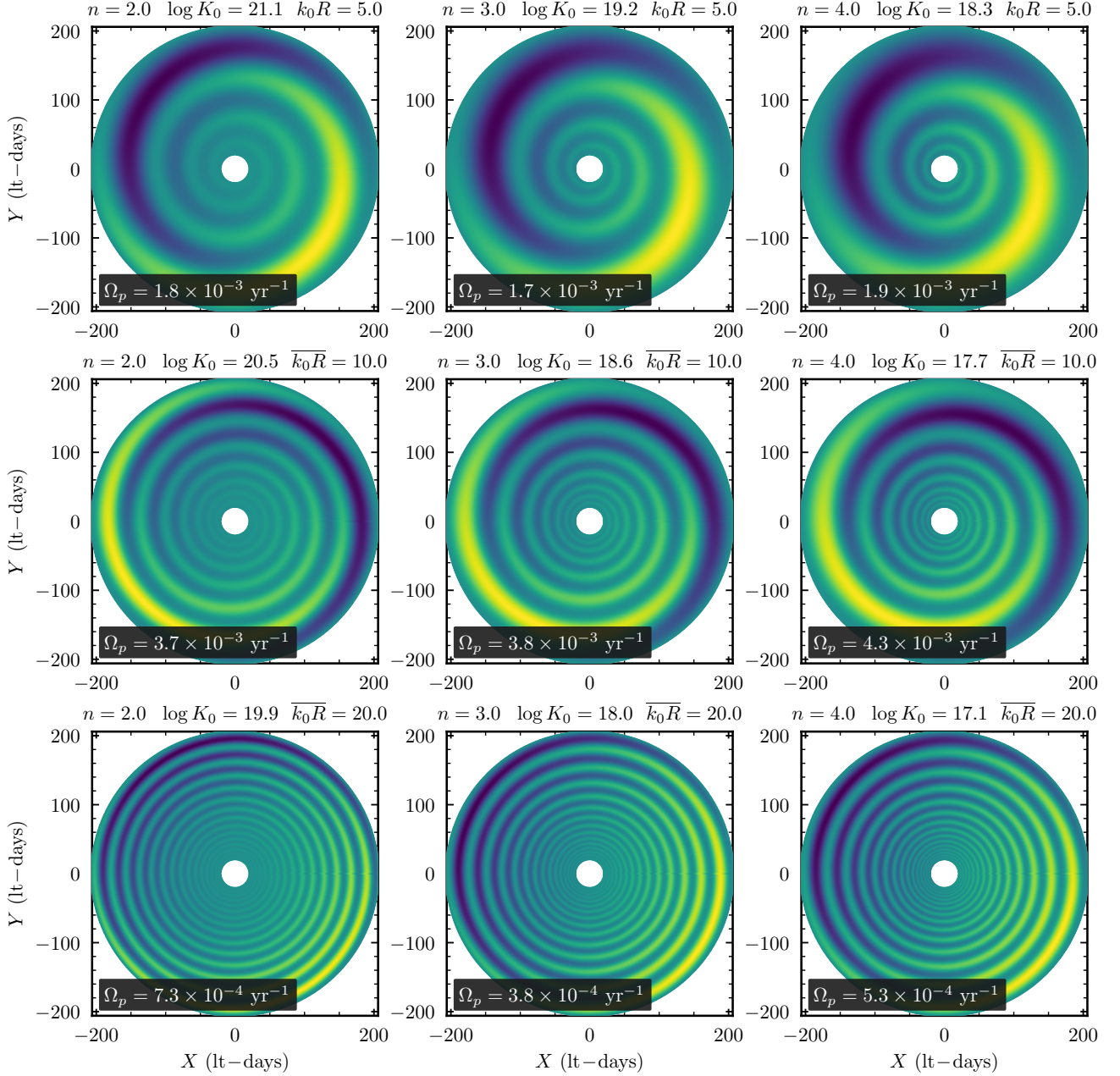


**Fig. 1.** The  $m = 1$  mode perturbations  $\sigma_1/\sigma_0$  for different parameters of equilibrium states. It generates one arm structure appearing as a crest (with colors from green to yellow) on an axisymmetric disk. The bright arm is undergoing reverberation with response to variations of ionizing continuum. The dark arm shows a density valley without or weakly response to the continuum variations.  $\Omega_p = \omega/m$  is the rotation speed of the arm pattern.

spectroastrometry with GRAVITY/VLTI can reach an unprecedentedly high spatial resolution of  $\sim 10\mu\text{as}$ . It had been successfully applied to 3C 273 for the geometry and kinematics of its BLR (Gravity Collaboration et al. 2018)<sup>2</sup>. The spiral arms developed from density waves may show some signatures that can be detected by GRAVITY/VLTI. The detailed scheme for spectroastrometry technique is described in Rakshit et al. (2015) and Songsheng et al. (2019). Below we outline a brief description for the sake of completeness. Given the surface brightness distribution, we have the photon center of the source at wavelength  $\lambda$

<sup>2</sup> Current accuracy of GRAVITY measurements of 3C 273 is only enough to test a simple disk model rather than sub-structures of spiral arms (see details of Gravity Collaboration et al. 2018).

$$\epsilon(\lambda) = \frac{\int \alpha O(\alpha, \lambda) d^2\alpha}{\int O(\alpha, \lambda) d^2\alpha}, \quad (18)$$

where  $O(\alpha, \lambda) = O_\ell + O_c$  is the surface brightness distribution of the source contributed by the BLR and continuum emissions, and  $\alpha$  is the angular displacement on the celestial sphere. Given the geometry and kinematics of a BLR, its  $O_\ell$  can be calculated for the broad emission line with the observed central wavelength  $\lambda_{\text{cen}}$  through

$$O_\ell = \int \frac{\Xi_R F_c}{4\pi R^2} f(\mathbf{R}, \mathbf{v}) \delta(\alpha - \alpha') \delta(\lambda - \lambda') d^3\mathbf{R} d^3\mathbf{v}, \quad (19)$$

where  $\lambda' = \lambda_{\text{cen}} \gamma_0 (1 + \mathbf{v} \cdot \mathbf{n}_{\text{obs}}/c) (1 - R_S/R)^{-1/2}$  includes the gravitational shift due to the central SMBH,  $R_S = 2R_g$  is the Schwarzschild radius,  $\gamma_0 = (1 - v^2/c^2)^{-1/2}$  is the Lorentz factor,  $\alpha' = [\mathbf{R} - (\mathbf{R} \cdot \mathbf{n}_{\text{obs}}) \mathbf{n}_{\text{obs}}] / D_A$ ,  $\mathbf{R}$  is the distance to the central SMBH,  $f(\mathbf{R}, \mathbf{v})$  is the velocity distribution of BLR clouds at  $\mathbf{R}$ , and  $F_c$  is the ionizing flux. By introducing the fraction of the emission-line flux to the total ( $\ell_l$ ), we have

$$\epsilon(\lambda) = \ell_l \epsilon_\ell(\lambda), \quad (20)$$

where

$$\epsilon_\ell(\lambda) = \frac{\int \alpha O_\ell d^2\alpha}{\int O_\ell d^2\alpha}, \quad \ell_l = \frac{F_\ell(\lambda)}{F_{\text{tot}}(\lambda)}, \quad F_\ell(\lambda) = \int O_\ell d^2\alpha, \quad (21)$$

and

$$F_{\text{tot}}(\lambda) = F_\ell(\lambda) + F_c(\lambda). \quad (22)$$

For an interferometer with a baseline  $\mathbf{B}$ , a non-resolved source, with a global angular size smaller than its resolution limit  $\lambda/B$ , has the interferometric phase

$$\phi_*(\lambda, \lambda_r) = -2\pi \mathbf{u} \cdot [\epsilon(\lambda) - \epsilon(\lambda_r)], \quad (23)$$

where  $\mathbf{u} = \mathbf{B}/\lambda$  is the spatial frequency, and  $\lambda_r$  is the wavelength of a reference channel. Given the geometry and kinematics of the BLR, the spectroastrometric signals can therefore be calculated.

### 3. Results: SA and RM signals

It is known that the nearly-Keplerian disks dominated by the potential of central sources favor  $m = 1$  mode, namely a single spiral arm (Adams et al. 1989; Shu et al. 1990; Lee et al. 2019). We can obtain  $\omega$  from the eigenvalue problem of Equation (9) as well as the perturbed component ( $\sigma_1/\sigma_0$ ) for density waves. In this paper, we only focus on the general patterns of the arms for the nearly Keplerian rotating disks, and we leave their growth rates connected with the imaginary part of  $\nu = (\omega - \Omega)/\kappa$  in the second paper of this series (Du et al. 2022 in preparation).

The dispersion relation can be used to give a rough estimate to the tightness of winding of the spiral arms, which is expressed by  $(\omega - \Omega)^2 = \kappa^2 + k^2 a_0^2 - 2\pi G |k| \sigma_0$  (Lin & Lau 1979), we have

$$k = -k_0 \left[ 1 \pm \sqrt{1 - Q_{\text{disk}}^2 (1 - \nu^2)} \right], \quad k_0 = \frac{(2\pi G)^{1/2n} Q_{\text{disk}}^{(1-2n)/2n}}{K_0^{1/2} \Omega^{(1-n)/n}}. \quad (24)$$

Pitch angles of spiral arms are determined by  $\tan i = 1/kR$  for given  $n$ ,  $K_0$  and  $Q_{\text{disk}}$ , and  $k_0 R$  can be representative of the global pitch angles. In order to conveniently show the spiral arms, we use the proxy of pitch angles defined by  $\bar{k}_0 R = (R_{\text{out}} - R_{\text{in}})^{-1} \int_{R_{\text{in}}}^{R_{\text{out}}} k_0 R dR$  along the radial axis as an input parameter in following calculations, rather than  $K_0$ . Moreover, the validity of the tightly wound approximation can be obviously justified by this parameter. Given  $\mathcal{M}$  and  $M_\bullet$ , we show dependence of  $\bar{k}_0 R$  on  $K_0$  and  $n$  in Appendix C. In general, decreasing  $K_0$  and  $n$  leads to increases of  $\bar{k}_0 R$ , and  $\bar{k}_0 R$  slightly depends on  $\mathcal{M}$  and  $M_\bullet$ . This is caused by the dependence of inner and outer boundaries on  $\mathcal{M}$  and  $M_\bullet$ , see Eqn 12 and Appendix C. As a representative, we focus on the case with  $\mathcal{M} = 1.0$  and  $M_\bullet = 10^8 M_\odot$ , and  $Q_{\text{disk}} = 1$  in the present paper.

Figure 1 shows the spiral arms of several cases with different  $K_0$  and polytropic index  $n$  for  $m = 1$  mode. In this Figure, we arrange the panels in the same line have the same  $\bar{k}_0 R$ . The corresponding eigenvalues ( $\Omega_p = \omega/m$ ) are marked in the left corners in individual panels. Although the BLR gas may not be illuminated by the central ionizing radiation if  $n < 3$  (see more details in Section 2.1), we still show the cases with  $n = 2$  in Figure 1 for comparison. It is obvious that the arms wind more tightly if  $\bar{k}_0 R$  is larger. In addition, the contrast of the perturbations in the central regions becomes clearer if  $n$  increases.

Figure 2 shows the emission-line profiles of the case with  $n = 4$  and  $\bar{k}_0 R = 5.0$  (the arm pattern in the upper-right corner in Figure 1) for different azimuthal and inclination angles ( $\theta$  and  $i_0$ ) of the line of sight. The maximum value of  $\sigma_1/\sigma_0$  is fixed to be  $(\sigma_1/\sigma_0)_{\text{max}} = 0.2$ . The real situations may be smaller or larger than the value adopted here. The azimuthal angle  $\theta = 0^\circ$  refers to the line of sight that the observer looks the BLR pattern in Figure 1 from the right side, and the azimuthal angle increases counter-clockwise (the rotational velocity of gas is also counter-clockwise). For comparison, the profiles of the corresponding unperturbed disks without spiral arms are also superposed in Figure 2. As expected, the unperturbed disk (geometrically thin) structure of the BLR generates symmetric double-peaked profiles. The double peaks are blended if the disk tends to be observed from a face-on direction (e.g.,  $i_0 = 20^\circ$  in Figure 2). The line profiles of the disks with the spiral arms are obviously asymmetric. For example, in the cases with  $\theta = 45^\circ$ , the blue peaks are significantly higher than the red ones because the bright parts of the arms are approaching. As  $\theta$  increases from  $0^\circ$ , the asymmetry first becomes stronger until  $\theta \sim 45^\circ - 90^\circ$  and then gets weaker. The width of the line profile increases if the inclination angle increases. The differences between the profiles with and without spiral arms are also shown in Figure 2. If  $\sigma_1/\sigma_0$  is larger, the asymmetry of the profiles will become stronger, and vice versa.

In Figure 2, we also calculate spectroastrometric signals (orange lines), which are detectable for GRAVITY/GRAVITY+ on VLTI. The signals are significantly different from the standard  $S$ -curves. The  $S$ -curves of the unperturbed BLR disks are symmetric that the amplitudes of the blue and red peaks are the same. The phase curves of the BLR with the spiral arm for different azimuthal and inclination angles are also asymmetric just like their emission-line profiles. The differences between the perturbed and unperturbed BLR disks are also shown as the residuals in Figure 2. They are the functions of inclination and azimuthal angles. Comparing with the unperturbed BLR disk, the amplitudes of the blue troughs in the cases with the spiral arm are stronger and those of the red peaks become weaker. Similar to the line profiles, the asymmetry of the phase curve first increases if  $\theta$  becomes larger, and then decreases after  $\theta \sim 45^\circ - 90^\circ$ . The width of the phase curve increases with the inclination angle increasing. The current GRAVITY/VLTI can conveniently detect differential phase angles to  $\sim 0.1^\circ$ , and GRAVITY+ as its next generation<sup>3</sup> will definitely observe the features much weaker than the present in the near future.

Figure 3 shows the transfer functions (velocity-delay maps) of the spiral arm with  $n = 4$  and  $\bar{k}_0 R = 5$  for different azimuthal and inclination angles. For a brief comparison with the present, we refer readers to the figures showing the transfer functions of Keplerian disks in Welsh & Horne (1991) and Wang et al. (2018). A Keplerian disk shows a symmetric bell-like fea-

<sup>3</sup> see more details from [https://www.mpe.mpg.de/7480772/GRAVITYplus\\_WhitePaper.pdf](https://www.mpe.mpg.de/7480772/GRAVITYplus_WhitePaper.pdf)



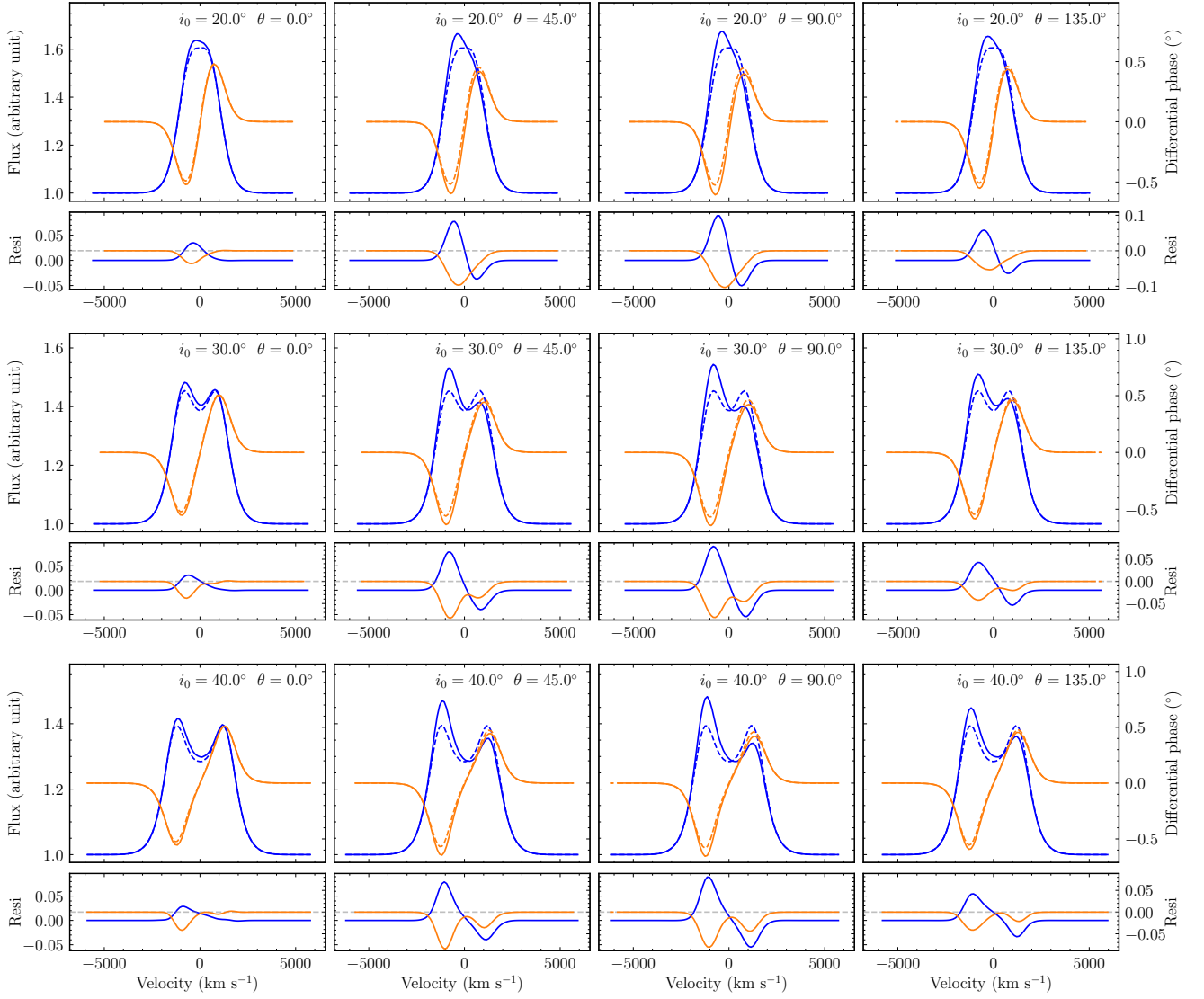


**Fig. 2.** Characterized profiles of BLR-disk ( $\sigma_0 + \sigma_1$ ) with one-arm structure (in blue) and differential phase curves (in orange). The panels are for different orientation and azimuthal angles. Dashed-lines represent emission from an homogeneous disk, and the solid lines from the disk with spiral-arm. In the calculations, we take the perturbations of surface density  $(\sigma_1/\sigma_0)_{\max} = 0.2$ . The differences between the solid and dashed lines are provided as residuals with the corresponding colors. The differential phases can be measured by GRAVITY, and the residual to the homogenous disk can be also detected for the BLR with the present parameters. Less massive black holes can be measured by GRAVITY+ (the next generation of GRAVITY).

ture. For clarity, in Figure 3, we only plot the response of the density perturbations ( $\sigma_1$ ). For comparison, an example of the transfer function for the unperturbed disk is shown by Figure D.1 in Appendix D. As shown in Figure 3, the major influences of the spiral arm are the variations of the bell’s waist. We find that the higher and lower density perturbations (wave crest and wave trough, see also in Figure 1) generate positive and negative signals (stronger and weaker responses) with superposition to the transfer functions of Keplerian disks, respectively. Actually, there is some deficit of the right waist in the bell-like transfer function of NGC 5548 as shown in (Xiao et al. 2018). When  $\theta = 0^\circ$ , the positive signals are mainly located in near side (smaller time lags) and the negative signals tend to be at larger time lags. Along with  $\theta$  increasing from  $0^\circ$ , the positive and negative signals rotate clockwise. Measuring the rotation of the features is one of the keys to test the presence and dynamics of the spiral arms in BLRs.

For cases with  $Q_{\text{disk}} = 1 + \Delta Q$ , where  $\Delta Q < 0.3$ , we have done the calculations and found the general patterns of arms do not change significantly for given  $k_0 R$ . We omit the figures.

## 4. Discussions

### 4.1. Tight-winding approximation

Employing the traditional WKB approximation (e.g., Lin & Lau 1979), we for the first time apply the theory of density waves to BLRs for broad emission line profiles, differential phase curves, and velocity-delay maps. The validity of this approximation can be simply estimated by comparing the global pitch angle proxy of  $k_0 R$  as shown in Figure 1 with detailed calculations in Du et al. (2022 in preparation) which relaxes the WKB approximation for the more loosely wound cases. We find that the difference of pitch angles can be less than  $\lesssim 20\%$  for  $\overline{k_0 R} = 5$ . It is generally

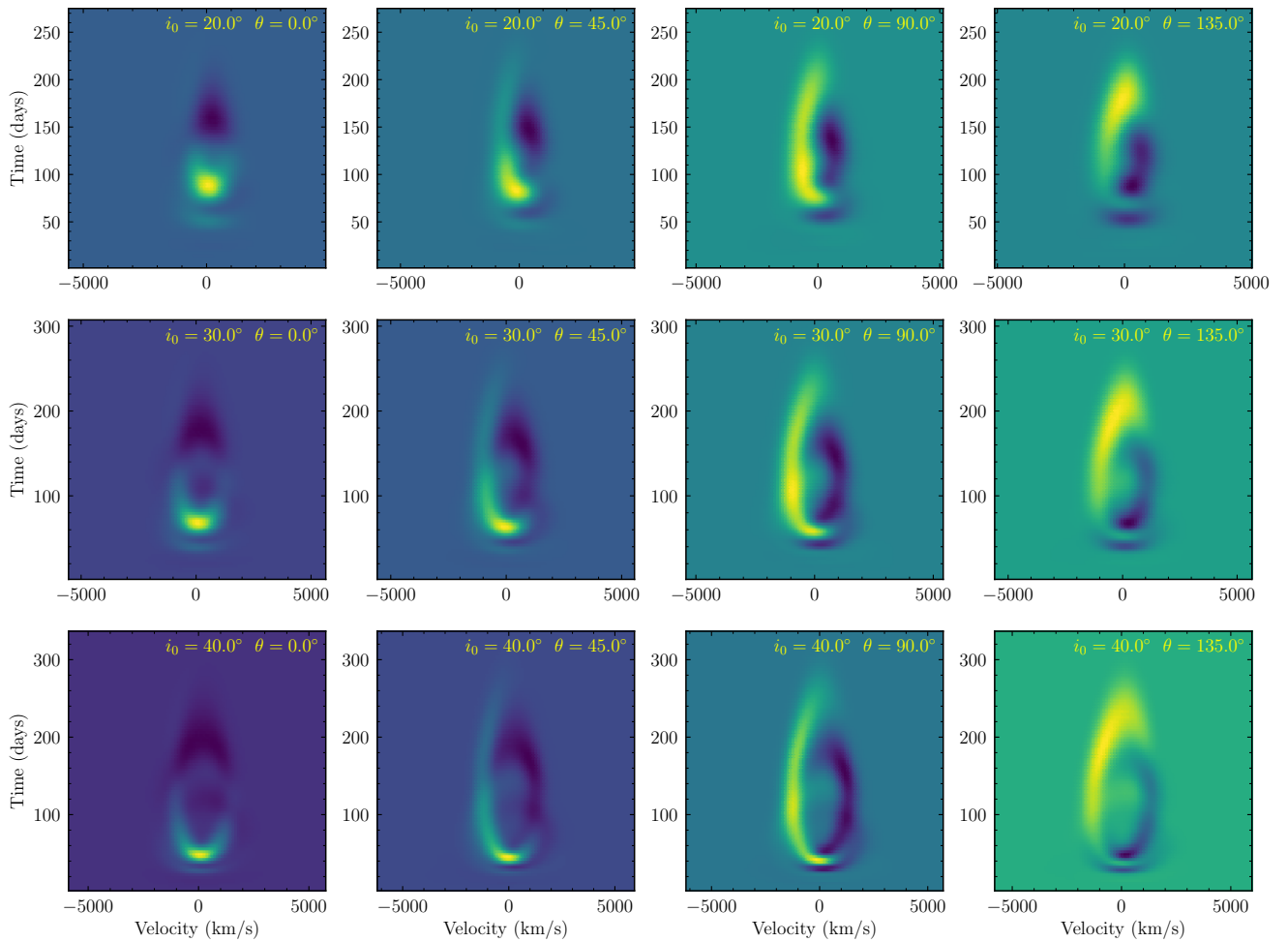


**Fig. 3.** Velocity-delay maps  $[\Psi(v, t)]$  of the spiral arms for the case with  $n = 4$  and  $\overline{k_0 R} = 5$ . For clarity, we only plot the response of the density perturbations ( $\sigma_1$ ). The color codes the strength of  $\Psi(v, t)$  (brighter for stronger and darker for weaker responses).

believed the WKB approximation is good enough for  $\overline{k_0 R} \gtrsim 5$ , which is consistent with Lin & Lau (1979).

Moreover, the non-linear effects have been extensively studied by Lee & Goodman (1999), who draw a conclusion that single-armed density waves can exist even in nearly Keplerian disks with only weak self-gravity. Pitch angle of the arms can be significantly larger with non-linear effects. Relaxing the WKB approximation schemed by Adams et al. (1989) will generate more general results for AGN BLR issues as shown in a forthcoming paper (Du et al. 2022 in preparation). On the other hand, some simulations show that  $m = 1$  is also favored when the disk mass is comparable with the central SMBHs (e.g., Lodato & Rice 2004; Kratter & Lodato 2016). In such a context, the disk will be thicker than the present cases so that the Poisson equation has more complicated expression than Eqn. (8). Density waves will be modified by radial self-gravity of the disks.

#### 4.2. Observational appearance

The present profiles of broad emission lines can be conveniently compared with observations. The suggested spiral arms for asymmetric profiles of some AGNs (e.g., Eracleous & Halpern 1994; Storchi-Bergmann et al. 2017) could originate from the results of self-gravity instability. Observational appearance should be tested by examining individual AGNs and statistic properties. Asymmetric profiles of Palomar-Green quasars are common, and

statistically, the asymmetries are significantly correlated with the strengths of Fe II (which clearly depends on accretion rates  $\mathcal{M}$ ; see Figure 5 in Boroson & Green 1992). This has a clear implication that the homogeneity of ionized gas distributions is governed by accretion rates. Marziani et al. (2003, 2009, 2010) investigated the line profiles of low- and intermediate-redshift AGNs, and concluded that the line asymmetry changes systematically along the so-called quasar “eigenvector 1 sequence”. Parameters of  $n$ ,  $K_0$ , and  $Q_{\text{disk}}$  may dependent directly on  $\mathcal{M}$  in reality, resulting in the dependence of the arms on accretion rate. This could probably explain these phenomena. We also note that asymmetries of H $\beta$  profiles are changing with time from red to blue asymmetries or reverse, which could be naturally explained by the pattern motion of  $m = 1$  mode spiral arms. High fidelity RM of AGNs, that employs high spectral resolution and homogeneous cadence, will finally reveal sub-structures of the BLRs through detailed 2D transfer functions from response to the ionizing sources (Welsh & Horne 1991; Horne et al. 2004; Wang et al. 2018; Songsheng et al. 2019, 2020) as well as the spectroastrometric observations of GRAVITY/VLTI with the predicted characteristics. Detailed comparisons with observations will be deferred to a future paper.

However, the true situation can be more complicated than the simplified model adopted here, which could make the density waves (spiral arms) more complex, especially in the cases of radiation pressure-driven warped disks (Pringle 1996), MRI-



driven turbulence or other instabilities (e.g., a brief review in Ogilvie & Latter 2013), or star formation (Shlosman & Begelman 1989; Collin & Zahn 1999; Gammie 2001; Collin & Zahn 2008; Wang et al. 2011, 2012). Magnetic fields could be very important in some cases. Moreover, fast cooling could make the disk suffer from violent instability, condense into discrete clouds, and even generate filamentary spiral pattern (e.g., Gammie 2001; Rice et al. 2003, 2011; Kratter & Lodato 2016; Brucy & Hennebelle 2021). However, on one hand, heating caused by MRI or radiation from inner region may balance the cooling effect. On the other hand, from the perspective of observation, high-resolution spectroscopy in Arav et al. (1997, 1998) provides a lower limit to the number of clouds in BLRs and exclude that BLRs consist of “discrete” clouds. Whatever how complicated the physics is in BLRs, future detections will advance understanding the mystery of the BLRs.

#### 4.3. Relation between BLR and accretion disk

The origin of BLRs and their relation with accretion disks are still a puzzle. In the present paper, we assume that the BLR is the illuminated surface layer of the accretion disk (in the SG region). Such kind of assumption was also adopted by, e.g., Goad et al. (2012). Only in  $n > 3$  cases, the gas on the surface can be illuminated by the central ionizing photons. It should be noted that radiation pressure from the disk may puff up the height of this region (e.g., Emmering et al. 1992; Murray et al. 1995; Chiang & Murray 1996; Czerny & Hryniewicz 2011; Elvis 2017; Baskin & Laor 2018) and provide a covering factor that is large enough to explain the BLR observations, which will ease the restriction of polytropic index. However, more thick disk may potentially stabilize against non-axisymmetric perturbation and reduce the lifetime of spiral arms (Ghosh & Jog 2021). The observation in Horne et al. (2021) has indicated the azimuthal structures in BLRs, which gives a constraint that the lifetime of the arms cannot be too short. The influence of the thick BLR layers should be investigated both theoretically and observationally in future.

#### 4.4. Self-gravity of the accretion disks

To maintain density waves needs  $Q_{\text{disk}} \sim 1 - 1.3$  (e.g., Lodato & Rice 2004) driven by several mechanisms mentioned in Section 1, however, it is expected to distinguish them from observations. Star formation in the self-gravitating disks could support the state of  $Q_{\text{disk}}$  as suggested by (e.g., Shlosman & Begelman 1989; Collin & Zahn 1999; Thompson et al. 2005; Wang et al. 2011). As a self-regulation, higher star formation will decrease the surface density of the disks increasing  $Q_{\text{disk}}$  whereas lower star formation rates increase the surface density decreasing  $Q_{\text{disk}}$ . Except for releases of gravitational energy of accreting gas, star formation and supernovae explosion will supply additional energies to this region. As independent evidence for this, fortunately, AGNs and quasars are known to be metal-rich providing observational constraints on these processes. It would be interesting to test potential dependence of broad emission line profiles on the metallicity ( $Z$ ). As hint evidence, asymmetries of  $H\beta$  profiles strongly correlate with  $\text{Fe II}$  strength ( $\mathcal{R}_{\text{Fe}}$ ) (see Figure 5 in Boroson & Green 1992) while  $\mathcal{R}_{\text{Fe}}$  is a proxy of accretion rates (e.g., Boroson & Green 1992; Marziani et al. 2003; Hu et al. 2012; Shen & Ho 2014) correlating with  $Z$ .

Finally, self-gravity has been neglected in vertical direction of the BLR for its height (i.e., in the equation of  $H = a_0 \Omega^{-1}$ ). A sophisticated treatment of the vertical structure will include self-

gravity as well as radiation pressure from viscosity dissipation and star formation (and supernovae explosion). We leave this in a future paper.

## 5. Conclusions

There is growing evidence for appearance of spiral arms in broad-line regions of active galactic nuclei. In this paper, using the WKB approximation, we start from the perturbation equations to study dynamics and structures of ionized gas in the SG regions around SMBHs, which constitute the major parts of BLRs. We calculate the major properties of density waves excited by the  $m = 1$  mode. The features of density waves can be detected by asymmetric profiles, differential interferometric signals (by GRAVITY/GRAVITY+ onboard VLTI), and 2D transfer functions from RM campaigns. In particular, the patterns of spiral arm in the 2D transfer functions are unique due to rotation motion of spiral arm.

These features help to better understand the physical connection between SG disks and BLRs in AGNs. Using the hypothesis that SG regions maintain the Toomre constant  $Q \sim 1$ , we show that the excited density waves arising from perturbations of SG disks are responsible for inhomogeneous distributions of BLRs. It is possible to observationally test density waves in BLRs with the current instruments. Our preliminary results show that density waves in BLRs provide a new avenue for studying BLR structures and dynamics as well as for resolving the long-standing issues of BLRs.

*Acknowledgements.* We are grateful to an anonymous referee for a large number of comments and suggestions from a helpful report to improve the manuscript. We acknowledge the support by National Key R&D Program of China (grants 2016YFA0400701), by NSFC through grants NSFC-11991054, -11991051, -12022301, -11873048, -11833008, -11573026, and by Grant No. QYZDJ-SSW-SLH007 from the Key Research Program of Frontier Sciences, CAS, by the Strategic Priority Research Program of the Chinese Academy of Sciences grant No.XDB23010400.

## Appendix A: Basic equations

We start from the ideal fluid equations in the cylindric coordinates  $(R, \varphi, z)$ . For reader's convenience, we list the classical equations which can be found from Lau & Bertin (1978), Lin & Lau (1979) and Binney & Tremaine (2008). The continuity equation reads

$$\frac{\partial \sigma}{\partial t} + \frac{1}{R} \frac{\partial}{\partial R}(R\sigma u) + \frac{1}{R} \frac{\partial}{\partial \varphi}(\sigma v) = 0, \quad (\text{A.1})$$

and the motion equations are

$$\frac{\partial u}{\partial t} + u \frac{\partial u}{\partial R} + \frac{v}{R} \frac{\partial u}{\partial \varphi} - \frac{v^2}{R} = -\frac{\partial}{\partial R}(\mathcal{V}_0 + \psi + h), \quad (\text{A.2})$$

and

$$\frac{\partial v}{\partial t} + u \frac{\partial v}{\partial R} + \frac{v}{R} \frac{\partial v}{\partial \varphi} + \frac{uv}{R} = -\frac{1}{R} \frac{\partial}{\partial \varphi}(\psi + h), \quad (\text{A.3})$$

where  $\mathcal{V}_0$  is the potential. We should mention that the viscosity is neglected in above equations. This is valid for the quasi-Keplerian rotation disk as in the standard disk model (Shakura & Sunyaev 1973).

## Appendix B: Coefficients

The coefficients are given by follows

$$\mathcal{A} = -\frac{1}{R} \frac{d \ln \mathcal{A}}{d \ln R}, \quad \mathcal{A} = \frac{\kappa^2(1 - v^2)}{\sigma_0 R}, \quad v = \frac{\omega - m\Omega}{\kappa}; \quad (\text{B.1})$$

$$\mathcal{B} = -\frac{m^2}{R^2} - \frac{4m\Omega(Rv')}{\kappa R^2(1 - v^2)} + \frac{2m\Omega}{R^2 \kappa v} \frac{d \ln(\kappa^2/\sigma_0 \Omega)}{d \ln R}, \quad C = -\frac{\kappa^2(1 - v^2)}{a_0^2}. \quad (\text{B.2})$$

## Appendix C: Wave numbers of spiral arms

We present the dependence of  $\overline{k_0 R}$  on the parameter  $K_0$  and the polytropic index  $n$  in Figure C.1.  $\overline{k_0 R}$  decreases with  $K_0$  and  $n$  increase. In addition,  $\overline{k_0 R}$  increases slightly if  $\mathcal{M}$  and  $M_\bullet$  increase. The current dependence on  $\mathcal{M}$  and  $M_\bullet$  in the present model is mainly caused by the dependence of the inner and outer boundaries on these two parameters (see Eqn 12). In reality,  $K_0$ ,  $n$ , and even  $Q_{\text{disk}}$  may rely on  $\mathcal{M}$  and  $M_\bullet$  more directly.

## Appendix D: An example of the transfer function for unperturbed disk

In Figure 3 of Section 3, we present the transfer functions of the spiral arms ( $\sigma_1$ ). Here, for comparison, we provide an example of the transfer function of the unperturbed disk ( $\sigma_0$ ) in Figure D.1.

## References

Adams, F. C., Ruden, S. P. & Shu, F. H. 1989, *ApJ*, 347, 959  
 Antonucci, R. 1993, *ARA&A*, 31, 473  
 Arav, N., Barlow, T. A., Laor, A., et al. 1997, *MNRAS*, 288, 1015  
 Arav, N., Barlow, T. A., Laor, A., et al. 1998, *MNRAS*, 297, 990  
 Bahcall, J. N., Kozlovsky, B.-Z. & Salpeter, E. E., 1972, *ApJ*, 171, 467  
 Barth, A. J., Bennert, V. N., Canalizo, G., et al. 2015, *ApJS*, 217, 26  
 Balbus, S. A. & Hawley, J. F. 1998, *Reviews of Modern Physics*, 70, 1

Baldwin, J., Ferland, G., Korista, K., et al. 1995, *ApJ*, 455, L119  
 Baldwin, J. A., Ferland, G. J., Korista, K. T. et al. 2003, *ApJ*, 582, 590  
 Baskin, A. & Laor, A. 2018, *MNRAS*, 474, 1970  
 Barth, A. J., Pancoast, A., Bennert, V. N., et al. 2013, *ApJ*, 769, 128  
 Beckers, J. M. 1982, *Optica Acta*, 29, 361  
 Bentz, M. C., Walsh, J. L., Barth, A. J., et al. 2009, *ApJ*, 705, 199  
 Bentz, M. C., Walsh, J. L., Barth, A. J., et al. 2010, *ApJ*, 716, 993  
 Bentz, M. C., Denney, K. D., Grier, C. J., et al. 2013, *ApJ*, 767, 149  
 Bertin, G. 2014, *Dynamics of Galaxies*, by Giuseppe Bertin, Cambridge, UK: Cambridge University Press, 2014  
 Binney, J. & Tremaine, S. 2008, *Galactic Dynamics: Second Edition*, by James Binney and Scott Tremaine. ISBN 978-0-691-13026-2 (HB). Published by Princeton University Press, Princeton, NJ USA, 2008.  
 Blandford, R. D. & McKee, C. F. 1982, *ApJ*, 255, 419  
 Boroson, T. A. & Green, R. F. 1992, *ApJS*, 80, 109  
 Bottorff, M., Korista, K. T., Shlosman, I. & Blandford, R. D. 1997, *ApJ*, 479, 2000  
 Brucy, N. & Hennebelle, P. 2021, *MNRAS*, 503, 4192  
 Chiang, J. & Murray, N. 1996, *ApJ*, 466, 704  
 Collin, S. & Zahn, J.-P. 1999, *A&A*, 344, 433  
 Collin, S. & Zahn, J.-P. 2008, *A&A*, 477, 419  
 Combes, F., García-Burillo, S., Audibert, A. et al. 2019, *A&A*, 623, A79  
 Czerny, B., & Hryniewicz, K. 2011, *A&A*, 525, L8,  
 Dehghanian, M., Ferland, G., Peterson, B. M. et al. 2019, *ApJ*, 882, L30  
 Denney, K. D., Peterson, B. M., Pogge, R. W., et al. 2009, *ApJ*, 704, L80  
 Denney, K. D., Peterson, B. M., Pogge, R. W., et al. 2010, *ApJ*, 721, 715  
 Du, P., Hu, C., Lu, K.-X., et al. 2014, *ApJ*, 782, 45  
 Du, P., Lu, K.-X., Hu, C., et al. 2016a, *ApJ*, 820, 27  
 Du, P., Lu, K.-X., Zhang, Z.-X., et al. 2016b, *ApJ*, 825, 126  
 Du, P., Zhang, Z.-X., Wang, K., et al. 2018a, *ApJ*, 856, 6  
 Du, P., Brotherton, M. S., Wang, K., et al. 2018b, *ApJ*, 869, 142  
 Du, P. & Wang, J.-M. 2019, *ApJ*, 886, 42  
 Elitzur, M. & Shlosman, I. 2006, *ApJ*, 648, L101  
 Elvis, M. 2017, *ApJ*, 847, 56  
 Emmering, R. T., Blandford, R. D., & Shlosman, I. 1992, *ApJ*, 385, 460  
 Eracleous, M. & Halpern, J. P. 1994, *ApJS*, 90, 1  
 Gammie, C. F. 2001, *ApJ*, 553, 174  
 Gámez Rosas I. V., Isbell, J. W., Jaffe, W. et al. 2022, *Nature*, 602, 403  
 Ghosh, S. & Jog, C. J. 2021, *arXiv:2111.10893*  
 Gilbert, A. M., Eracleous, M., Filippenko, A. V., et al. 1999, *Structure and Kinematics of Quasar Broad Line Regions*, 175, 189  
 Gravity Collaboration, Sturm, E., Dexter, J., et al. 2018, *Nature*, 563, 657  
 Gravity Collaboration, Pfuhl, O., Davies, R. et al. 2020, *A&A*, 634, A1  
 Gravity Collaboration, Amorim, A., Bauböck, M., et al. 2020, *A&A*, 643, A154  
 Gravity Collaboration, Amorim, A., Bauböck, M., et al. 2021, *A&A*, 648, A117  
 Grier, C. J., Peterson, B. M., Pogge, R. W. et al. 2012, *ApJ*, 755, 60  
 Grier, C. J., Peterson, B. M., Horne, K. et al. 2013, *ApJ*, 764, 47  
 Grier, C. J., Peterson, B. M., Horne, K., et al. 2013, *ApJ*, 764, 47  
 Goad, M. R., Korista, K. T., & Ruff, A. J. 2012, *MNRAS*, 426, 3086  
 Goodman, J. 2003, *MNRAS*, 339, 937  
 Goodman, J. & Tan, J. 2004, *ApJ*, 608, 108  
 Ho, L. C. 2008, *ARA&A*, 46, 475  
 Horne, K., Peterson, B. M., Collier, S. J., et al. 2004, *PASP*, 116, 465  
 Horne, K., De Rosa, G., Peterson, B. M., et al. 2021, *ApJ*, 907, 76  
 Hu, C., Wang, J.-M., Ho, L. C. et al. 2012, *ApJ*, 760, 126  
 Imanishi M., Nakanishi K., Izumi T., Wada K., 2018, *ApJ*, 853, L25  
 Impellizzeri C. M. V. et al., 2019, *ApJ*, 884, L28  
 Kaspi, S., Smith, P. S., Netzer, H., et al. 2000, *ApJ*, 533, 631  
 Königl, A. & Kartje, J. F. 1994, *ApJ*, 434, 446  
 Korista, K., Baldwin, J., Ferland, G., et al. 1997, *ApJS*, 108, 401  
 Korista, K. T. & Goad, M. R. 2000, *ApJ*, 536, 284  
 Koshida, S., Minezaki, T., Yoshii, Y., et al. 2014, *ApJ*, 788, 159  
 Korycansky, D. G. & Pringle, J. E. 1995, *MNRAS*, 272, 618  
 Kratter, K. & Lodato, G. 2016, *ARA&A*, 54, 271  
 Lau, Y. Y. & Bertin, G. 1978, *ApJ*, 226, 508  
 Lee, E. & Goodman, J. 1999, *MNRAS*, 308, 984  
 Lee, W.-K., Dempsey, A. M. & Lithwick, Y. 2019, *ApJ*, 882, L11  
 Li, Y.-R., Songsheng, Y.-Y., Qiu, J., et al. 2018, *ApJ*, 869, 137  
 Li, Y.-R., Xiao, M. & Wang, J.-M. 2021, *ApJ*, 921, 151  
 Lin, C. C. & Shu, F. 1964, *ApJ*, 140, 646  
 Lin, C. C. & Shu, F. H. 1966, *Proceedings of the National Academy of Science*, 55, 229  
 Lin, C. C. & Lau, Y. Y., 1979, *StAM*, 60, 97  
 Lin, D. N. C. & Pringle, J. E. 1987, *MNRAS*, 225, 607  
 Lodato, G. & Rice, W. K. M. 2004, *MNRAS*, 351, 630  
 Lodato, G. 2007, *Nuovo Cimento Rivista Serie*, 30, 293  
 Lu, K.-X., Wang, J.-G., Zhang, Z.-X. et al. 2021, *ApJ*, 918, 50  
 Lubow, S. H. & Ogilvie, G. I. 1998, *ApJ*, 504, 983  
 Lynden-Bell, D. 1969, *Nature*, 223, 690  
 Lyu, J., Rieke, G. Smith, P. S. 2019, *ApJ*, 886, 33  
 Marziani, P., Zamanov, R. K., Sulentic, J. W., et al. 2003, *MNRAS*, 345, 1133

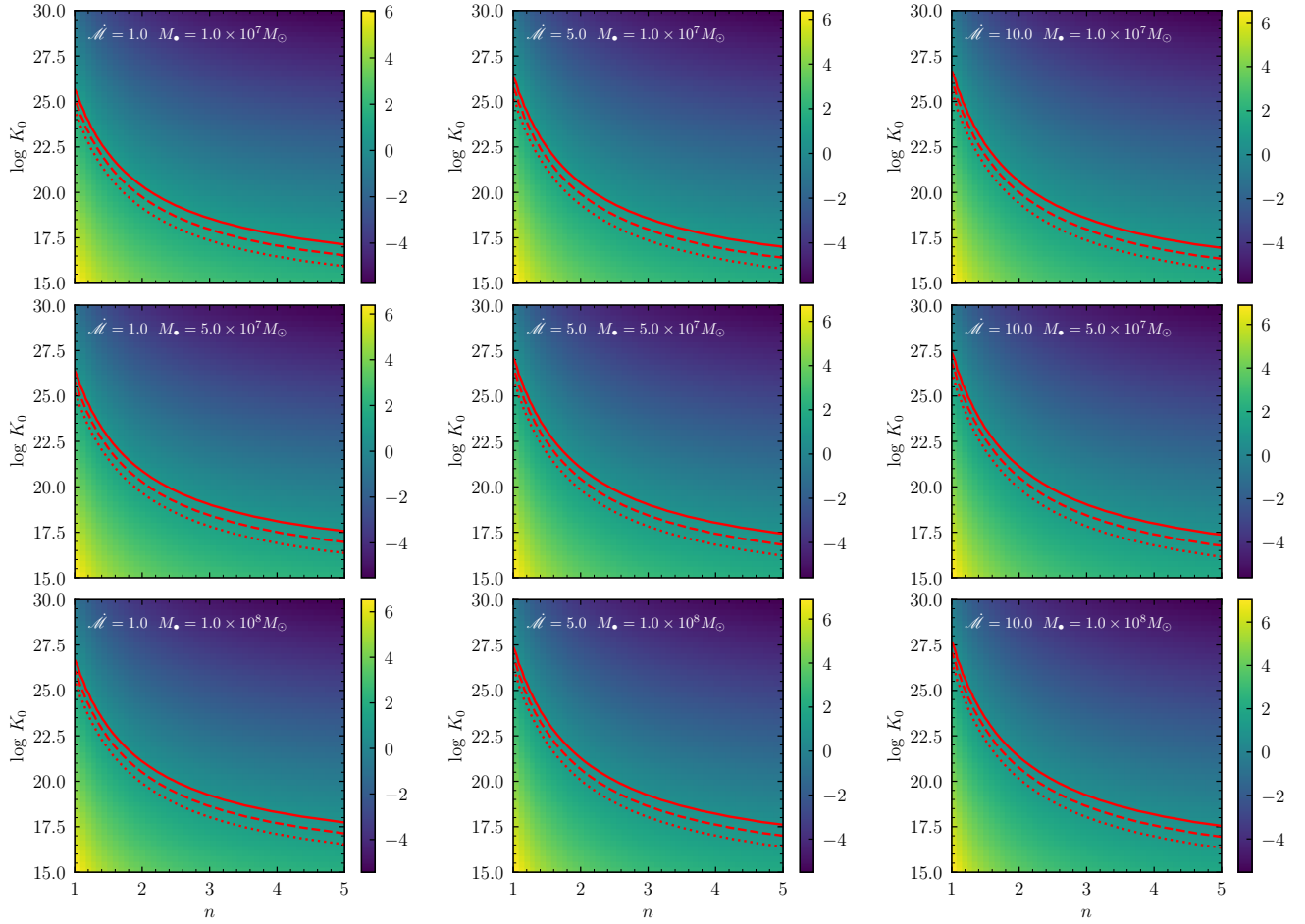


**Fig. C.1.**  $\overline{k_0 R}$  as a function of  $K_0$  and  $n$ . The color represents the logarithmic value of  $\overline{k_0 R}$ . The red solid, dashed, and dotted lines represent  $\overline{k_0 R} = 5, 10, 20$ , respectively (corresponding to the cases in Figure 1).

- Marziani, P., Sulentic, J. W., Stirpe, G. M., et al. 2009, *A&A*, 495, 83  
 Marziani, P., Sulentic, J. W., Negrete, C. A., et al. 2010, *MNRAS*, 409, 1033  
 Minezaki, T., Yoshii, Y., Kobayashi, Y. et al. 2019, *ApJ*, 886, 150  
 Murray, N., Chiang, J., Grossman, S. A., et al. 1995, *ApJ*, 451, 498  
 Nenkova, M., Sirocky, M. M., Ivezić, Ž. et al. 2008, *ApJ*, 685, 147  
 Netzer, H. 2013, *The Physics and Evolution of Active Galactic Nuclei*, by Hagai Netzer, Cambridge, UK: Cambridge University Press, 2013  
 Netzer, H. & Laor, A. 1993, *ApJ*, 404, L51  
 Ogilvie, G. I. & Latter, H. N. 2013, *MNRAS*, 433, 2403  
 Osterbrock, D. E. & Ferland, G. J. 2006, *Astrophysics of Gas Nebulae and Active Galactic Nuclei* (Mill Valley, CA: Univ. Science Books)  
 Paczynski, B. 1978a, *Acta Astron.*, 28, 91  
 Paczynski, B. 1978b, *Acta Astron.*, 28, 241  
 Pancoast, A., Brewer, B. J., Treu, T., et al. 2014, *MNRAS*, 445, 3073  
 Pei, L. AGN STORM Collaboration 2017, *ApJ*, 837, 131  
 Peterson, B. M. 1993, *PASP*, 105, 247  
 Peterson, B. M. & Wandel, A. 2000, *ApJ*, 540, L13. doi:10.1086/312862  
 Peterson, B. M., Ferrarese, L., Gilbert, K. M., et al. 2004, *ApJ*, 613, 682  
 Peterson, B. M., Wanders, I., Bertram, R., et al. 1998, *ApJ*, 501, 82  
 Petrov, R. G. *Differential Interferometry*, in *NATO Advanced Science Institutes (ASI) Series C*, 1989, ed. D. M. Alloin & J. M. Mariotti 274, 249.  
 Pringle, J. 1996, *MNRAS*, 281, 357  
 Rafikov, R. R. 2015, *ApJ*, 804, 62  
 Rakshit, S., Petrov, R. G., Meilland, A. & Hönig, S. F. 2015, *MNRAS*, 447, 2420  
 Rice, W. K. M., Armitage, P. J., Bate, M. R., et al. 2003, *MNRAS*, 339, 1025  
 Rice, W. K. M., Armitage, P. J., Mamatsashvili, G. R., et al. 2011, *MNRAS*, 418, 1356  
 Salpeter, E. E. 1964, *ApJ*, 140, 796  
 Seyfert, K. 1943, *ApJ*, 97, 28  
 Shakura, N. I. & Sunayev, R. A. 1973, *A&A*, 24, 337  
 Shen, Y. & Ho, L. C. 2014, *Nature*, 513, 210  
 Shen, Y., Grier, C. J., Horne, K. et al. 2019, *ApJ*, 883, L14  
 Shlosman, I. & Begelman, M. C. 1989, *ApJ*, 341, 685  
 Sirko, E. & Goodman, J. 2003, *MNRAS*, 341, 501  
 Songsheng, Y.-Y., Wang, J.-M., & Li, Y.-R. 2019, *ApJ*, 883, 184  
 Songsheng, Y.-Y., Xiao, M., Wang, J.-M. & Ho, L. C. 2020, *ApJS*, 247, 3  
 Shu, F. H. 2016, *ARA&A*, 54, 667  
 Shu, F. H., Tremaine, S., Adams, F. C. & Ruden, S. P. 1990, *ApJ*, 358, 495  
 Storchi-Bergmann, T., Nemmen da Silva, R., Eracleous, M., et al. 2003, *ApJ*, 598, 956  
 Storchi-Bergmann, T. et al., *ApJ*, 2017, *ApJ*, 835, 236  
 Suganuma, M., Yoshii, Y., Kobayashi, Y., et al. 2006, *ApJ*, 639, 46  
 Thompson, T. A., Quataert, E. & Murray, N. 2005, *ApJ*, 630, 167  
 Toomre, A. 1964, *ApJ*, 139, 1217  
 Tremaine, S. 2001, *AJ*, 121, 1766  
 U, V., Barth, A. J., Vogler, H. A., et al. 2022, *ApJ*, 925, 52  
 Vanden Berk, D. E., Richards, G. T., Bauer, A., et al. 2001, *AJ*, 122, 549  
 Wang, J.-M., Du, P., Baldwin, J. A., Ge, J.-Q., Hu, C. & Ferland, G. 2012, *ApJ*, 746, 137  
 Wang, J.-M., Ge, J.-Q., Hu, C., Baldwin, J. A. et al. 2011, *ApJ*, 739, 3  
 Wang, J.-M., Du, P., Brotherton, B. et al. 2017, *Nature Astronomy*, 1, 775  
 Wang, J.-M., Songsheng, Y.-Y., Li, Y.-R. & Yu, Z. 2018, *ApJ*, 862, 171  
 Welsh, W. F. & Horne, K. 1991, *ApJ*, 379, 586  
 Williams, P. R., Pancoast, A., Treu, T. et al. 2020, *ApJ*, 902, 74  
 Woltjer, L. 1959, *ApJ*, 130, 38  
 Xiao, M., Du, P., Lu, K.-K., et al. 2018, *ApJ*, 865, L8,  
 Zel'Dovich, Y. B. 1965, *Soviet Astronomy*, 9, 221

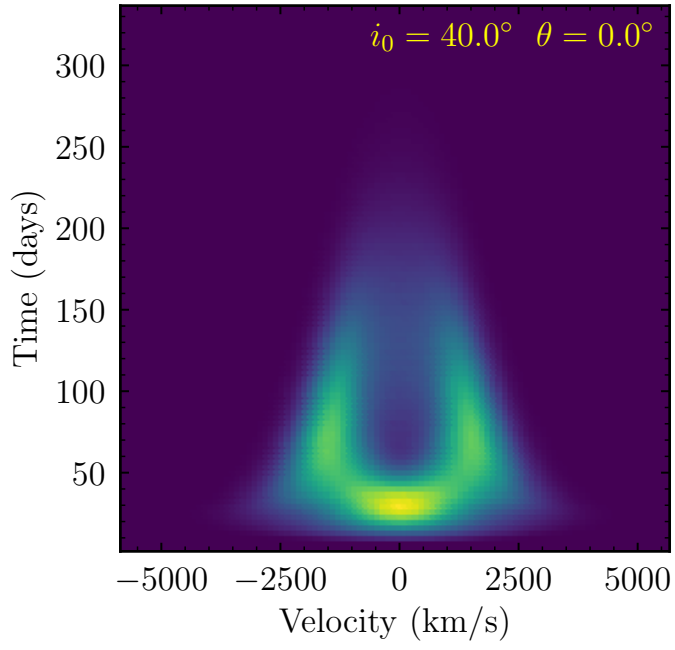


**Fig. D.1.** An example of the transfer function for unperturbed disk ( $\sigma_0$ ).